New Journal of Physics
The open access journal at the forefront of physics

Deutsche Physikalische Gesellschaft DPG IOP Institute of Physics

PAPER • OPEN ACCESS

Anisotropic x-ray scattering and orientation fields in cardiac tissue cells

To cite this article: M Bernhardt *et al* 2017 *New J. Phys.* **19** 013012

New Journal of Physics
The open access journal at the forefront of physics

Deutsche Physikalische Gesellschaft DPG
IOP Institute of Physics

Published in partnership with: Deutsche Physikalische Gesellschaft and the Institute of Physics

OPEN ACCESS

RECEIVED
5 August 2016

REVISED
11 October 2016

ACCEPTED FOR PUBLICATION
20 October 2016

PUBLISHED
12 January 2017

PAPER

Anisotropic x-ray scattering and orientation fields in cardiac tissue cells

M Bernhardt[1], J-D Nicolas[1], M Eckermann[1], B Eltzner[2], F Rehfeldt[3] and T Salditt[1,4]

[1] Institut für Röntgenphysik, Georg-August-Universität Göttingen, Friedrich-Hund-Platz 1, Göttingen D-37077, Germany
[2] Institut für Mathematische Stochastik, Georg-August-Universität Göttingen, Goldschmidtstrasse 7, Göttingen D-37077, Germany
[3] Drittes Physikalisches Institut-Biophysik, Georg-August-Universität Göttingen, Friedrich-Hund-Platz 1, Göttingen D-37077, Germany
[4] Author to whom any correspondence should be addressed.

E-mail: rehfeldt@physik3.gwdg.de **and** tsaldit@gwdg.de

Keywords: protein fibers, actin, cardiomyocytes, small-angle x-ray scattering, x-ray focussing, nano-diffraction

Supplementary material for this article is available online

Abstract

X-ray diffraction from biomolecular assemblies is a powerful technique which can provide structural information about complex architectures such as the locomotor systems underlying muscle contraction. However, in its conventional form, macromolecular diffraction averages over large ensembles. Progress in x-ray optics has now enabled to probe structures on sub-cellular scales, with the beam confined to a distinct organelle. Here, we use scanning small angle x-ray scattering (scanning SAXS) to probe the diffraction from cytoskeleton networks in cardiac tissue cells. In particular, we focus on actin-myosin composites, which we identify as the dominating contribution to the anisotropic diffraction patterns, by correlation with optical fluorescence microscopy. To this end, we use a principal component analysis approach to quantify direction, degree of orientation, nematic order, and the second moment of the scattering distribution in each scan point. We compare the fiber orientation from micrographs of fluorescently labeled actin fibers to the structure orientation of the x-ray dataset and thus correlate signals of two different measurements: the native electron density distribution of the local probing area versus specifically labeled constituents of the sample. Further, we develop a robust and automated fitting approach based on a power law expansion, in order to describe the local structure factor in each scan point over a broad range of the momentum transfer q_r. Finally, we demonstrate how the methodology shown for freeze dried cells in the first part of the paper can be translated to alive cell recordings.

1. Introduction

Biological cells can be treated as active non-equilibrium states of soft-matter, with a surprising versatility in structure, dynamics and function [12–15]. Force generation in muscle cells is a perfect example of how biomolecular structures and dynamics in cells enable unique functionality. Providing the forces required for heart muscle contraction, cardiomyocytes (CMs) are well known to develop a highly ordered cytoskeletal architecture comprising acto-myosin assemblies arranged in the sarcomeric structures of myofibrils. A quantitative understanding also of the dynamical properties often is proceeded by detailed structural analysis. For example, the basic principle to establish contractile forces has been elucidated by multiple seminal works starting in the 1950s, relying on the combination of phase contrast imaging, electron microscopy (EM) and x-ray diffraction [16, 17] also covering first time resolved x-ray diffraction experiments on the frog muscle (*R. esculenta*) [3–5]. These classical experiments have led to an understanding of the basic principle of muscle contraction, culminating in the sliding filament theory [18, 19] and sophisticated cross-bridging models for a single power stroke [20–23]. However, at the time, limited state of the art x-ray focussing capabilities forced investigators to average over macroscopically large cell assemblies.

Recent progress in x-ray optics has now overcome this barrier, enabling hard x-ray spot sizes in the sub-micron range [24], well suited to record structural data within precise locations of a single cell. X-rays even in the multi-keV regime required for diffraction studies can nowadays be focussed by a variety of optical elements, including diffractive optics such as Fresnel zone plates [25], compound refractive lenses [26–28] and elliptical Kirkpatrick–Baez (KB) mirrors [29–32]. Similar to earlier scanning diffraction work on biomaterials such as wood and bone [33–38], we can hence now combine high resolution in reciprocal space with at least moderate resolution in real space. Scanning small angle x-ray scattering (scanning SAXS) experiments requiring a sample environment for biological cells are typically not compatible with the ultimate small spot sizes of 10 nm and below, as presented in [31, 39, 40], but values in the range of 80–300 nm are feasible, in particular in terms of the working distance, and readily allow structure factors to be assigned to different cellular compartments. Presently, feasibility of cellular scanning SAXS has been demonstrated for a variety of biological cells, ranging from bacterial cells *D. radiodurans* [6] to eukaryotes such as the amoeba *D. discoideum* [10], adenoma cells [7–9, 41], and human mesenchymal stem cells (hMSC) [11].

Beyond these previous proof-of-concept experiments and experimental feasibility studies, what is the potential of scanning SAXS for the investigation of biological cells, and what could be its role within the plethora of other imaging techniques?

Scanning SAXS complements the repertoire of imaging techniques [42]: it is less limited in terms of sample preparation than EM enabling the stuctural analysis of biological cells in various preparation states. Independent of any labeling such as for fluorescence-based microscopy, scanning SAXS detects all cellular constituents present in proportion to the respective electron density contrast and distribution. For cellular experiments, structural attributes down to an equivalent structure size of a few nanometers can thus be detected [7, 10, 11].

While the diffraction pattern may in many cases not be conclusive by visual inspection, they in principle encode a wealth of structural information [43], which can be interpreted in view of the detailed biomolecular structures and assemblies in different cellular compartments. In order to 'decode' these signals, elaborate analysis algorithms, as well as supporting simulations and eventually coherent imaging techniques (e. g. ptychography, holography and tomography [6, 44]) are required to 'invert' the diffraction signal. More importantly, many structures will not be identifiable or interpretable without correlative investigations with other high resolution imaging techniques [43], for example super-resolution optical microscopy such as PALM and STED [45–49].

In this work, we demonstrate how conventional fluorescence microscopy can be correlated and applied jointly with the novel scanning SAXS capabilities, for quantitative comparison of the cytoskeleton structure. At the same time, we show that data-driven quantification for example of the local orientations of the scattering signal and its correlation to optical fluorescence of labeled protein networks reveals already significant information, even prior to model-based analysis. From a more general point of view, quasi-vector fields of the local structural orientations within a cell as an active soft-matter system can quantify important polarization properties of the cell [14] as well as the response to mechanical cues [12, 13]. As a long term goal, once that correlative approaches between different imaging modalities have been achieved, the structural information should be linked to mechanical properties, in particular to stress and strain fields.

Figure 1(a) illustrates the basic components of a scanning SAXS experiment, and figure 1(b) the particular implementation at the Göttingen instrument for nano-imaging with x-rays (GINIX) [50] of the P10 beamline (PETRAIII/DESY), showing the sample together with the optical components, as further detailed in section 2. Figure 1(c) illustrates the typical data, which can be recorded in scanning SAXS experiments from cells, placing individual diffraction patterns on the grid of the scan. The example shown was recorded with the micro-SAXS setup of the cSAXS beamline (SLS/PSI), with a stepsize of $\Delta = 10\ \mu$m, much larger than the step sizes used at the GINIX instrument which are typically around $\Delta = 1\ \mu$m. The real space resolution of such a scan is hence moderate, but sufficient to assign the diffraction patterns to local structures. Importantly, however, the reciprocal space resolution, as determined from the decay of the diffraction signal to the noise level, is in the order of a few nanometers, as further detailed in SI, section 11.

This manuscript is organized as follows: after this introduction, instrumental settings and sample preparation are described in section 2, followed by the presentation of analysis approaches to correlate visible light fluorescence and anisotropic x-ray diffraction in section 3, including also first micro-SAXS results. This is further extended in section 4 to nano-focus SAXS datasets, demonstrating the resolution capabilities of recent SAXS experiments both in real and reciprocal space. Azimuthally averaged local structure factors of micro- and nano-SAXS signals are considered in section 5 and treated by automated batch fitting analysis. Statistical analysis of a large area scan is presented in section 6, regarding cell type specific structural parameters deduced from the automatized analysis of diffraction pattern [11]. Furthermore, principal component analysis (PCA) results are compared and correlated to the visible light fluorescence data. Preliminary results on alive cells are presented in section 7, before the manuscript closes with a brief summary and conclusion in section 8.

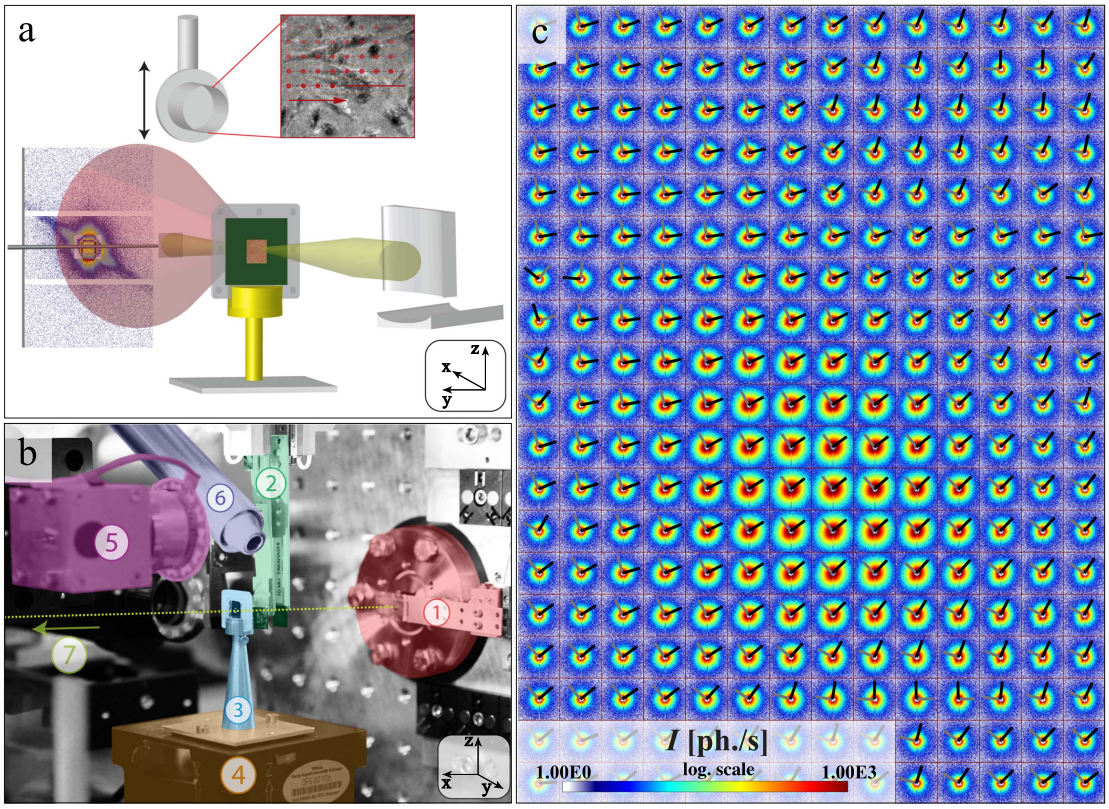

Figure 1. (a) Schematic of a scanning SAXS experiment with the basic instrumental components. (b) Photograph of the nano-focus setup GINIX at the P10 beamline (PETRAIII/DESY), with the sample chamber (blue) positioned in the focal plane of the focussing mirror system. The optical axis is marked as a yellow dash line. (c) Composite image showing diffraction patterns recorded in a coarse scan with stepsize $\Delta = 10\ \mu$m. The scattering signal is shown up to a momentum transfer of $q_{max} \approx 0.11\ \text{nm}^{-1}$. The principal axes as determined by a principal component analysis (PCA) are indicated as black and gray arrows. This scan region is further analyzed in section 3.

2. Materials and methods

2.1. Sample preparation

Cell culture: Highly transmissive silicon rich nitride windows (membrane thickness: 1 μm, Silson, UK) serving as substrates were plasma-cleaned, covered with about 20 μl coating solution (0.08% gelatine, 0.5% fibronectin in sterile H_2O) and incubated for typically 2 h (37 °C, 5% CO_2). Neonatal rat cardiac tissue cells (NRCTCs) were obtained from isolated hearts of neonatal wild-type rats without the atrium. Hearts were perfused with phosphate buffered saline (PBS), their cells were enzymatically disassembled, resuspended in nutrition medium (DMEM-F12 with low glucose, 10% FCS, 1% Penicillin/Streptomycin) [51, 52] and then transferred onto the coated substrates either by adequately placing a drop of cell suspension or by submersing the substrate in a suspension-flooded well. In case of the former, cells were allowed to settle before wells were flooded with nutrition medium. Samples were incubated overnight, sometimes for several days and monitored at different steps of the preparation procedure, also recording fluorescence micrographs of entire samples before plunging and after the lyophilization procedure (Zeiss Observer.Z1, Germany). *Sample fixation, labeling and lyophilization*: Samples were fixated using 4% paraformaldehyde or 9% formaldehyde in PBS, permeabelized (Triton X-100), washed and the actin network as well as the nucleus were labeled (using Hoechst 33342 & Phalloidin-A488, Invitrogen, USA). For cryogenic fixation, samples were washed with volatile buffer (85.6 mM triethylammonium acetate in H_2O) and then vitrified by rapid plunging into a cold bath of liquid ethane/propane mixture (typically about −195°) using a Leica EM grid plunging system (Leica Microsystems, Germany). Samples were transferred into liquid nitrogen and placed in a vacuum chamber in order to sublimate the remaining amorphous water layer. The chamber remained sealed until the sample had reached almost room temperature (typically after three days). Samples were transferred into a desiccator and stored in the dark until the x-ray recording. *Alive samples*: Cells were settled on the flat lid of the Silson wet chamber (top lid, Silson, UK), transferred into a 15 ml sealed vial filled with nutritium medium and delivered on time to the beamline using a mobile heat box (37 °C, delivering time: ≈5 h). On arrival, the sample was transferred back to a stationary incubator (37°C, 5% CO_2) in order to recover buffer capacities. Shortly before recording, the cell-containing lid

was transferred under a clean bench and the medium was replaced by a drop of ≈20 μl of degassed CO_2-independent medium (degassed by 20 min of sonification in vacuum) before closing the chamber, cleaning the outer window surface with water and start the x-ray recording.

2.2. X-ray setup

Nanofocus SAXS experiments were performed at the P10-beamline (PETRAIII/ DESY) using the GINIX instrumentation. The setting was as follows: a monochromatized x-ray beam (photon energy $E_{\text{ph.}} = 8$ keV, i. e. $\lambda_{\text{ph.}} \approx 154.9$ pm) was focussed by a set of KB mirrors to a spotsize of about 360 $\times$ 410 nm (horz.$\times$vert., FWHM, as determined by translation of a waveguide) probing the sample at its focal spot in approx. 20 cm distance from the second mirror. The primary beam was blocked by beamstops and scattered photons were recorded by a Pilatus 300 k pixelated single photon counting detector (Dectris, Switzerland) at about 5.1 m distance. A motorized piezo stage was used to scan the sample with respect to the beam. An on-axis visible light video microscope was used for navigation on the sample. An evacuated tube (not shown) spanned the sample-detector-distance significantly reducing air scattering. The following optical components are shown in figure 1(b): the exit of the evacuated KB box ①, two soft-edge apertures to trim the beam profile, and suppressing parasitic scattering caused by the KB-mirrors [53] ②, the sample wet chamber with highly transmissive x-ray windows (Silson, UK) [54] ③, the motorized translation stage ④, the on-axis video microscope ⑤, a cryostream used for cryogenic protection of freeze-dried and vitrified samples ⑥, and finally beamstops together with the evacuated tube and the detector (not shown) placed further downstream ⑦. The primary total flux as measured by the detector was $I_0 \approx 2.4 \times 10^{11}$ ph. s^{-1}.

Microfocus SAXS experiments were performed at the cSAXS-beamline of the Swiss Light Source (SLS/PSI) using a monochromized and moderately focussed x-ray beam with a photon energy of $E_{\text{ph.}} = 8.7$ keV corresponding to a wave length of $\lambda_{\text{ph.}} \approx 142.5$ pm. The beamsize was about 54 μm $\times$ 33 μm (horz. $\times$ vert., FWHM) at the sample position as determined by a scintillator based x-ray microscope. An on-axis optical microscope was used for orientation on the sample, stepping motors and a hexapod enabled translation of the sample during alignment and in scanning mode. A Pilatus 2 M single photon counting pixel detector [55] was positioned at approx. 7.5 m distance downstream from the sample position. An evacuated tube was used to minimize the background signal. The primary flux as measured on the detector was determined to $I_0 = 1.44 \times 10^{11}$ ph. s^{-1}.

3. Correlating fluorescence microscopy and scanning SAXS

While the SAXS patterns of many soft matter and biological samples are isotropic based on the large ensemble averages of structures in solution or tissues, one of the most striking observations when performing scanning SAXS on single cells is the pronounced anisotropy of the recorded diffraction patterns. This has become very apparent in recent studies of filamentous protein networks of the cytoskeleton [7–11], and can be confirmed by scanning *in vitro* (reconstituted) suspensions of filamentous actin [56] with sub-micron beams. This and the following section focus on the analysis of the anisotropic x-ray diffraction patterns by extracting characteristic quasi-vector fields by quantifying anisotropy parameters and correlate them to data obtained by visible light fluorescence microscopy. Note, that scanning SAXS records all contributions to the scattering signal (regardless of labeled or unlabeled constituents) within the probed spot, in contrast to visible light fluorescence microscopy, which shows only particularly labeled cytoskeletal components, here the actin network. However, the orientation of both signals is highly correlated, indicating the dominating effect of the filamentous elements to the observed diffraction patterns. To this end, a fluorescence micrograph of the actin-labeled sample was recorded after freeze-drying. Filaments with an intensity above a manually defined threshold were tracked by the filament-sensor published previously by Eltzner *et al* [57]. Post-processing these datasets led to a re-binning of the effective pixel size of the fluorescence image to match the independently chosen step size of the x-ray scan (here: $\Delta = 10$ μm). This enabled the correlation of fluorescence and x-ray data based observables.

Figure 2 illustrates this procedure by the example of the micro-SAXS scan presented in section 1: *a* first, the x-ray dark field is determined (semi-transparent top layer) representing the overall scattering intensity $I(a, b)$ at each scan position $(a, b) \in \mathbb{N}^2$ by integration of photon counts that do not belong to the primary beam or any instrument-related signal (see also SI section 11). Data are then correlated to the fluorescence micrograph (intransparent bottom layer). The relative translation between both images is estimated 'by eye' with an accuracy of about one scanning step size. Next, the (gray scaled) micrograph is analyzed leading to the detectable filaments shown in *b* (yellow lines). The corresponding orientation angles $\vartheta_{\text{fs}}(y, z)$ (fs: filament sensor) are then assigned to positions $(y, z) \in \mathbb{N}^2$ of the fluorescence image, see *c*. Pixels without filaments are set to the invalid orientation $\vartheta_{\text{fs}}(y, z) = -1°$ (see *c*, white color). This orientation map is then segmented into square blocks $B(a, b)$ with block size $L \times L$ (see *c*, red squares). Following Hotz *et al* [58], the intrinsic mean

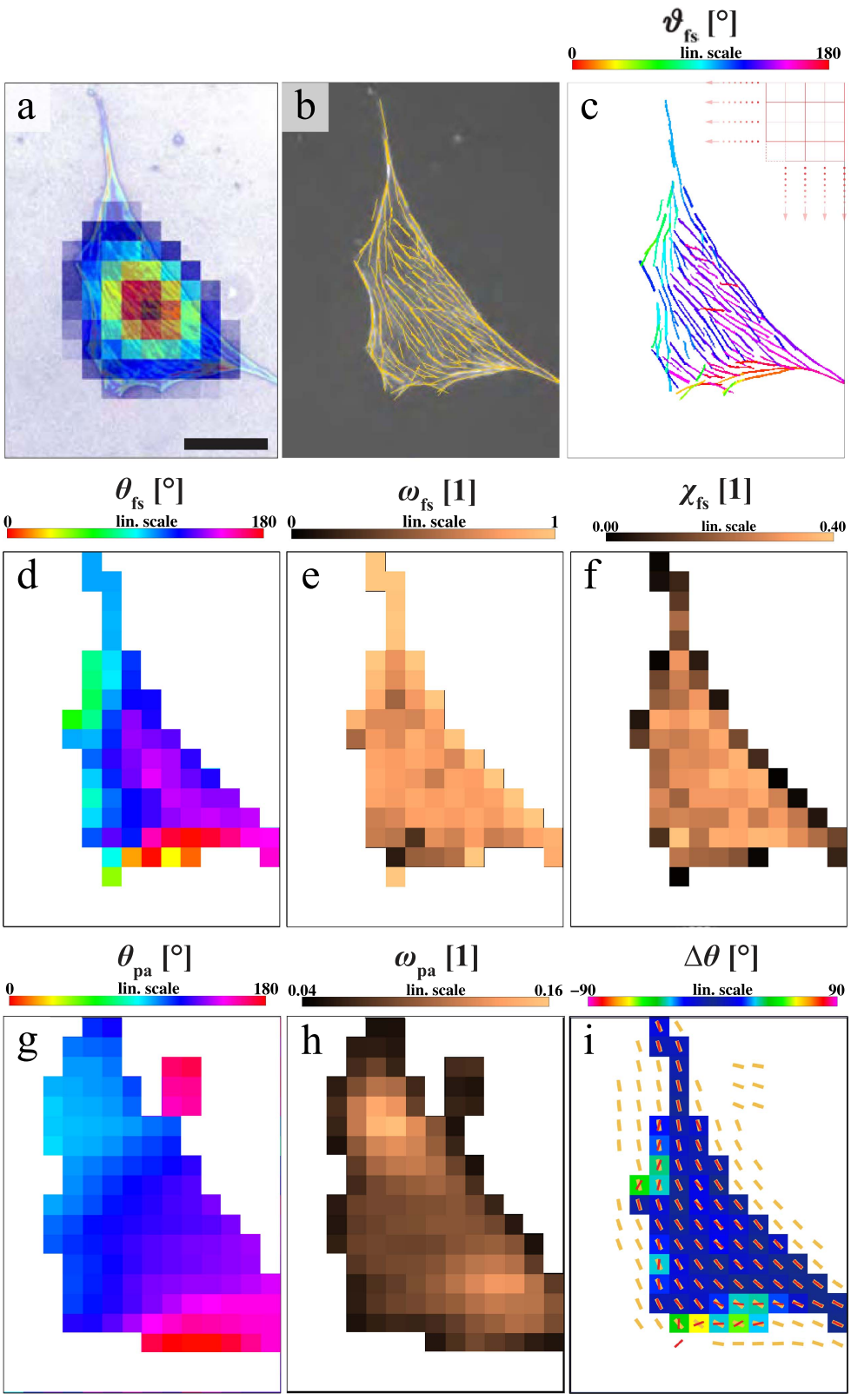

Figure 2. Comparative analysis of fluorescence microscopy and micro-SAXS for the cell presented in figure 1(a) : (a) correlative superposition of the x-ray dark field (semi-transparent top layer) and the unbinned fluorescence micrograph (intransparent bottom layer). Scalebar: 40 μm. (b) Gray-scaled fluorescence micrograph including all tracked filaments (yellow lines). (c) Unbinned orientation angles $\vartheta(y, z)$ for each pixel of the fluorescence image. The sequentially applied block size is indicated as red squares. White areas contain no tracked filaments. (d)–(f) The major three observables calculated for each block comprising (d) the mean orientation angle $\theta_{fs}(a, b)$, (e) the block polarization parameter $\omega_{fs}(a, b)$ and (f) the line order parameter $\chi_{fs}(a, b)$. (g) and (h) Orientation angle $\theta_{pa}(a, b)$, see (g), and anisotropy parameter $\omega_{pa}(a, b)$, see (*h*), as quantified by principal component analysis (PCA) of micro-SAXS diffraction patterns. (i) Discrepancy between orientation angles $\theta_{fs}(a, b)$ (thin red lines) and $\theta_{pa}(a, b)$ (thick yellow lines) as quantified by the angular deviation $\Delta\theta(a, b)$ (color code).

$\mu_{\text{int}}(a, b)$ and the variance $V_n(\mu_{\text{int}}(a, b))$ were calculated for each block: let $\tilde{B}(a, b) = \{(y, z) \in B(a, b), \vartheta_{\text{fs}}(y, z) \geqslant 0\}$ be the set and $N(a, b) = |\tilde{B}(a, b)|$ be the number of filament pixels within a block. Then orientation mean $\theta_{\text{fs}}(a, b)$ and variance $V_n(\mu_{\text{int}}(a, b))$ are defined as

$$f_{(a,b)}(\theta) := \sum_{(y,z)\in\tilde{B}(a,b)} \min(|\theta - \vartheta_{\text{fs}}(y, z)|, 180^\circ - |\theta - \vartheta_{\text{fs}}(y, z)|)^2, \tag{1}$$

$$\theta_{\text{fs}}(a, b) := \mu_{\text{int}}(a, b) = \underset{\theta\in[0^\circ,180^\circ)}{\operatorname{argmin}} f_{(a,b)}(\theta), \tag{2}$$

$$V_n(\mu_{\text{int}}(a, b)) = \min_{\theta\in[0^\circ,180^\circ)} f_{(a,b)}(\theta)/(N(a, b) - 1). \tag{3}$$

A block polarization parameter $\omega_{\text{fs}}(a, b)$ serves as a measure for the standard deviation in each segment and is given by

$$\omega_{\text{fs}}(a, b) = 1 - \frac{\sqrt{V_n(\mu_{\text{int}}(a, b))}}{90^\circ/\sqrt{3}} \tag{4}$$

with the variance $V_n(\mu_{\text{int}}(a, b))$ as defined in equation (3). The value $90^\circ/\sqrt{3}$ stems from the standard deviation of a uniform distribution on the circle.

A line order parameter $\chi_{\text{fs}}(a, b)$ is calculated as a measure for the amount of orientation-containing pixel inside a block

$$\chi_{\text{fs}}(a, b) = \frac{N(a, b)}{L^2}. \tag{5}$$

The resulting observables $\theta_{\text{fs}}(a, b)$, $\omega_{\text{fs}}(a, b)$ and $\chi_{\text{fs}}(a, b)$ for the micro-SAXS scan area are shown in figures 2(d)–(f). The corresponding x-ray diffraction patterns are analyzed based on PCA determining a structure orientation angle $\theta_{\text{pa}}(a, b)$, see *g*, and a unitless order parameter $\omega_{\text{pa}}(a, b)$ quantifying the anisotropic strength, see *h*. In the PCA treatment, the covariance matrix of the momentum transfer along q_y and q_z is computed for all photons, and after diagonalizing the matrix the corresponding eigenvectors $\vec{b}_1$ and $\vec{b}_2$ together with their eigenvalues λ_1 and λ_2 are determined, see [11] for full details. The degree of anisotropy is then computed as $\omega_{\text{pa}} = |\lambda_1 - \lambda_2|/(\lambda_1 + \lambda_2)$, reflecting the contributions of all anisotropic (i. e. aligned) scattering structures. For robustness, parameters are thresholded, considering only diffraction patterns with an ω_{pa}-value of $\omega_{\text{pa}} > 0.05$. Notably, the orientation angles $\theta_{\text{fs}}(a, b)$ and $\theta_{\text{pa}}(a, b)$ are directly comparable and indicate a surprisingly good agreement between fluorescence and x-ray diffraction data, which is remarkable if one keeps in mind the entirely different nature of the signals. This becomes more apparent when mapping the angular deviation

$$\Delta\theta(a, b) = \theta_{\text{fs}}(a, b) - \theta_{\text{pa}}(a, b) \tag{6}$$

for each pixel. Figure 2(i) shows the $\theta_{\text{fs}}(a, b)$ as thin red lines, $\theta_{\text{pa}}(a, b)$ as thick yellow lines and $\Delta\theta(a, b)$ for all accepted pixels as false color. Pixels which do not comprise both orientation angles (based on thresholding) are colored in white. Thresholding of x-ray data by $\omega_{\text{pa}}(a, b)$ can be justified *a posteriori*, since it reliably separates the cellular from the background signal in good agreement with the fluorescence image. Furthermore, as expected, micron sized beam dimensions cause noticable broadening of the signal beyond the cell's perimeter, leading to a putatively larger cellular area.

4. High resolution filament sensing

Towards a more localized structure analysis we have complemented micro-SAXS diffraction data by nanofocus SAXS experiments resulting in a 10–20× higher real space resolution. This enables the identification of different cellular compartments such as the nucleus of a cell. Figure 3 shows freeze-dried NRCTCs scanned with a step size of 0.5 μm. Figure 3(a) shows the x-ray dark field comprising clearly identifiable nucleic and cytoplasmic regions. As examples for the scattering patterns of different cellular areas, four locations have been selected (①–④), including next neighboring diffraction patterns:

Location ① shows nucleic diffraction patterns with the principle axes as found by PCA. These patterns exhibit an isotropic scattering distribution. Two horizontal lines and a white rectangle in the center region originate from the intermodular gaps of the detector and the fully absorbing beamstop, respectively. Locations ②–④ relate to three different cytoplasmic areas. In contrast to ①, numerous cytoplasmic diffraction patterns were found to have a pronounced anisotropic character enabling an accurate determination of the orientation angle $\theta_{\text{pa}}(a, b)$ of the scattering structures.

Following the procedure described above, fibers are tracked, here for a fluorescence micrograph acquired before plunging, yielding the orientation angles $\theta_{\text{fs}}(a, b)$ as shown in *b*. Note, that only the most significant filaments are detected, while the actin network is distributed over the entire cell area (see SI figure 6(a)). The

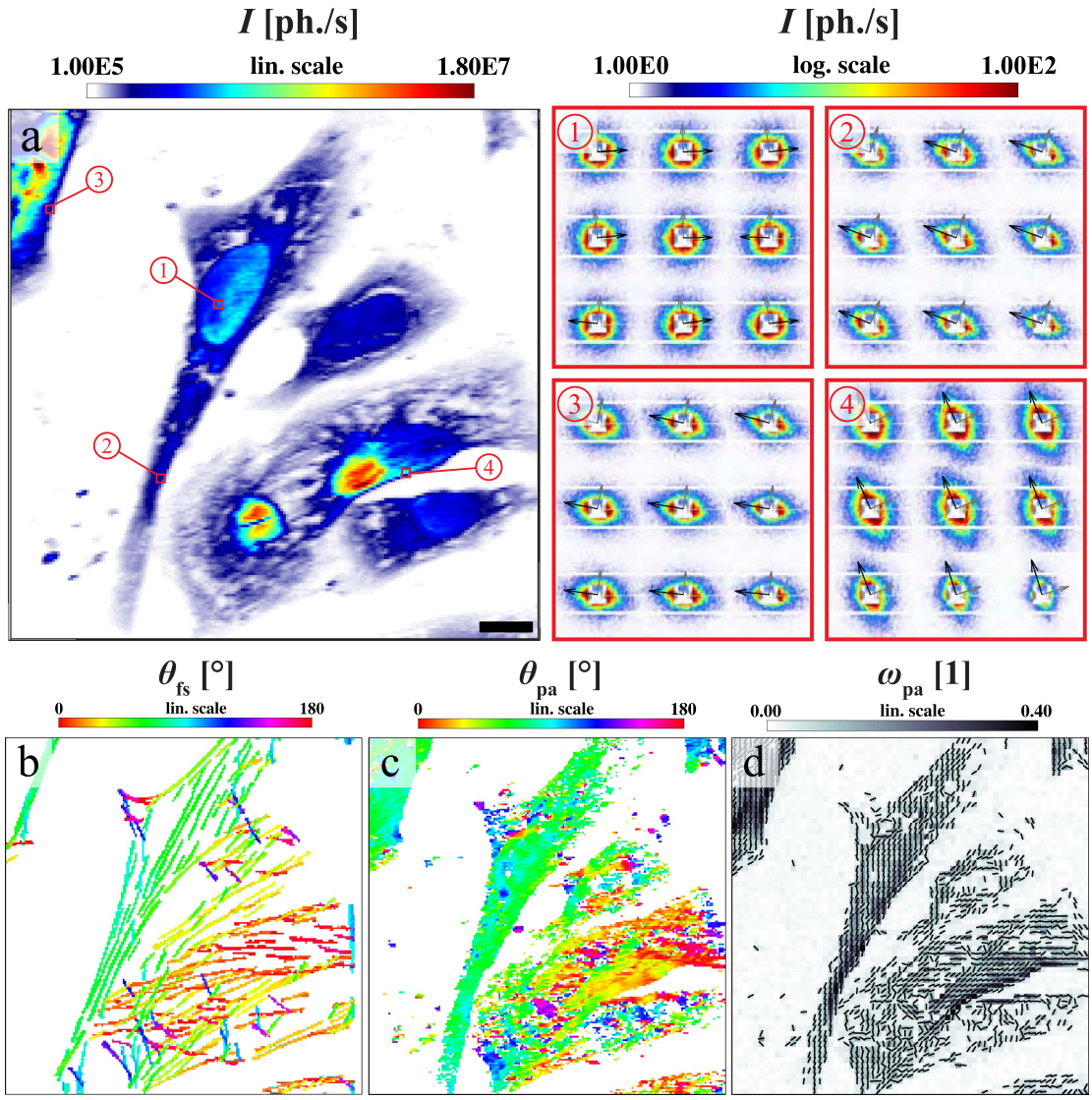

Figure 3. (a) Left: x-ray dark field representation of cardiac tissue cells scanned with a nano-focussed beam. Scalebar: 10 μm. Right: single diffraction patterns of selected regions as marked in the dark field, revealing isotropic patterns in nucleic (①) and anisotropic patterns in cytoplasmic regions (②–④) of the cells (the q-range shown here is up to $q_{max} \approx 0.45\ nm^{-1}$). (b) Orientation angles θ_{fs} of the most significant fibers, as determined from a corresponding micrograph of fluorescently labeled actin (only pixels above a manually defined threshold are shown). (c) Orientation angles θ_{pa} of diffraction patterns (only pixel with an order parameter $\omega_{pa} > 0.04$ are shown). (d) Mapping of PCA parameters with θ_{pa} as black lines and the order parameter ω_{pa} in gray scale. For clarity, only every third diffraction image is shown.

corresponding PCA results for θ_{pa} (a, b) are restricted to diffraction signals which exhibit an order parameter $\omega_{pa} > 0.04$, see (c). In line with previous observations, comparison of b and c reveal a high consistency between fluorescence microscopy and scanning SAXS. (d) The mapping of PCA results shows relatively high ω_{pa}-values in the order of $\omega_{pa} = 0.38$ which are perdominantly found on the perimeter or long extensions of cells. For presentation purposes only every third diffraction pattern is indicated.

5. Cellular structure factors

Analysis of radial intensity profiles $I(q_r)$ in SAXS typically involves model building based on form and structure factors. In view of the cytoskeletal filaments, which typically dominate the diffraction based on size, ordering and orientation, it seems reasonable to start with models of filament assemblies such as coarse grained helices composed of discrete spheres [59], form factors of intermediate filaments [60], actin helices [61, 62] or even effective filament bundles composed of Gaussian cylinders to model actin fiber bundles [10]. Of course, it is well understood that within the probed spot of a biological cell, a huge variety of molecular structures and assemblies contribute to the diffraction signal, so that a model based interpretation of $I(q_r)$ such as in *in vitro* solutions and suspensions is problematic in many instances. In the present case of CMs, a natural starting point would be the

models of the sarcomere inferred from macroscopic muscle diffraction. However, we did not yet find any indication for an ordered myofibril lattice corresponding to the well known sarcomeric structures.

This could be caused by several effects: a lower degree of ordered structures in the neonatal CMs studied, a loss of structure during preparation, a significantly lower signal-to-noise ratio than in muscle tissue, a convolution with the probing beam profile deviation from the typical plane wave geometry, or simple a problem of radiation damage. While it is difficult to discard any of these explanations, we continue with treating the observed diffraction signals. The observed curves $I(q_r)$ exhibit a monotonous decay with consistent asymptotic power-laws. In fact, as in many previous cellular SAXS data, especially at high q_r, the intensity profiles are often well described by a simple power-law

$$I_{\text{nano}}(q_r) = a \cdot q_r^b + c, \tag{7}$$

with an exponent typically within $-4.5 \leqslant b \leqslant -3$, while Porod's law for model particles with well-defined shapes and sharp interfaces is characterized by an exponent $b = -4$. Mapping the fitting parameters a–c could then eventually reveal different cellular compartments and cell types. Figure 4 shows the averaged radial intensity profiles $I(q_r)$ of selected cells as obtained for example by nano-SAXS scans (blue curves). A high real space resolution enables a separation of different cellular compartments, here resulting in background-corrected cytoplasmic and nucleic intensity profiles with fitting parameters listed in table 1.

While the simple power-law fit is sufficient for data recorded within a small q_r-range in particular in the Porod-regime, data with broader q_r-range require more elaborate fitting models. In this work, we have deliberately sacrificed real space resolution in one beamtime (cSAXS instrument), by scanning with a micro-focussed instead of a nano-focussed beam, in order to obtain a larger q_r-range, not interrupted by the tails of a highly diverging beam. While a separation into nucleic and cytoplasmic regions is not possible for these datasets due to the large beam size, this data did not suffer from the q_r-limitations caused by beam divergence and a consequentially larger overly sized beamstop of the nano-SAXS scans.

Figure 4 gives one example of a broad q_r-range signal (orange curves) also revealing a cross-over region (kink) at $q_r \approx 0.03\ \text{nm}^{-1}$. Such signals can be described adequatly by a more complex ansatz

$$I_{\text{micro}}(q_r) = \frac{1}{(a_1 \cdot q_r^{\beta} + a_2 \cdot q_r^{2\beta})^{2/\beta}} + b, \tag{8}$$

exhibiting a cross-over from -2 to a -4 exponent. The high q_r regime is thus in line with the nano-SAXS results and earlier experiments on freeze-dried eukaryotic cells [7, 10]; fit results are listed in table 2. Both of the fitting functions used above serve their purpose (in the respective q_r-ranges) reasonably well. However, analyzing large entities of local profiles in an automated manner requires a robust fitting algorithm, which should not be sensitive to starting values. Therefore, we replace nonlinear fitting of selected curves (by hand) with a linear fit by a linear combination of fixed ansatz functions. We found that an expansion q_r^p with fixed integer exponents p was highly suitable for the current data, i.e.

$$I_{\text{auto}}(q_r) = \sum_{p=-\infty}^{\infty} c_p \cdot q_r^p, \quad p \in \mathbb{Z}. \tag{9}$$

In fact, we find that for $I_{\text{auto}}(q_r)|_{p\in[-8,0]}$, all local intensity profiles are well-described (see SI, section 14), restricting equation (9) to

$$I_{\text{auto}}(q_r) = \sum_{p=-8}^{0} c_p \cdot q_r^p, \tag{10}$$

This approach reduces the tremendous amount of scattering data points of a scan to nine observables $c_{-8} - c_0$, while the expansion is entirely empirical and in particular does not result from any particular model. Importantly, these observables allow the computation of further parameters derived from the diffraction lineshapes (intensities, derivatives, inflection points, power law exponents, cross-over or moments) in an efficient manner. Obvious choices are the zeroth (i. e. the intensity) and the second momentum $F_0(q_r)$ and $F_2(q_r)$

$$F_0(q_r) = \int_{q_{\min}}^{q_{\max}} I_{\text{auto}}(q_r)\, \mathrm{d}q = c_0 + \left(c_{-1} \cdot \ln(q_r) + \sum_{i=-8}^{-2} \frac{1}{i+1} c_i \cdot q_r^{i+1} \right) \Bigg|_{q_r=q_{\min}}^{q_{\max}}, \tag{11}$$

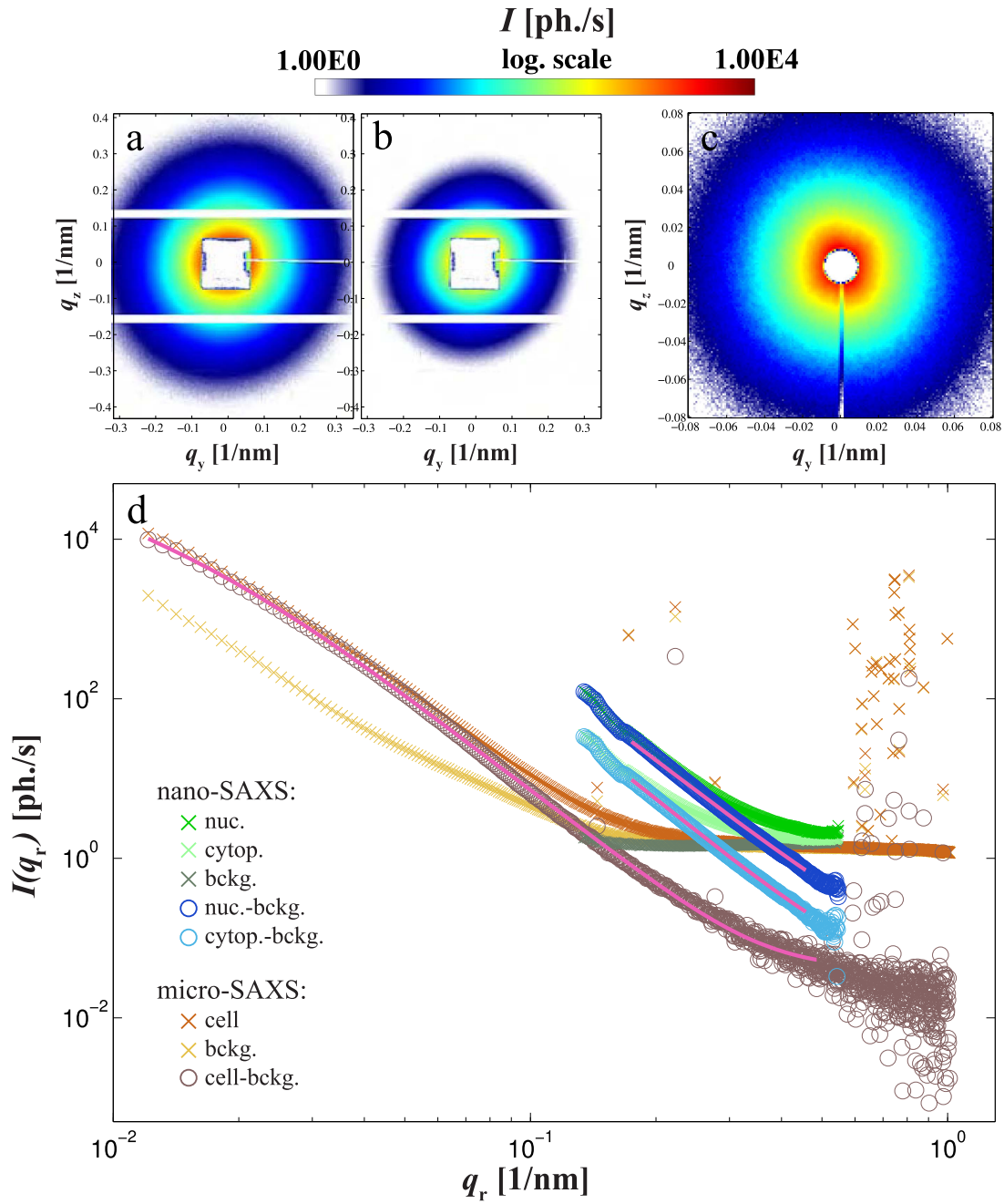

Figure 4. (a)–(c) Averaged and background-corrected 2D diffraction patterns of (a) the nucleus, and (b) the cytoplasm from a nano-SAXS scan, as well as (c) the center region of the detector of a cellular area from a micro-SAXS scan. (d) The corresponding radial intensity profiles $I(q_r)$ resulting from the azimuthal integration of these signals. Nucleic, cytoplasmic and background signals are shown for the nano-SAXS, as well as cellular and background signals for the micro-SAXS data.

Table 1. Fit results for a simple power-law according to equation (7) for a nano-SAXS data.

	a (ph. nm^b s^{-1})	b [1]	c (ph. s)
nuc.-bckg.	2.8×10^{-2}	−3.98	8.4×10^{-2}
cytop.-bckg.	6.6×10^{-3}	−4.17	3.9×10^{-2}

Table 2. Fit results for power-law with cross-over according to equation (8) for micro-SAXS data.

	a_1 $[\frac{\mathrm{nm}^{\beta_s/2}}{\mathrm{ph.}^{\beta/2}}]$	a_2 $[\frac{\mathrm{nm}^{2\beta_s/2}}{\mathrm{ph.}^{\beta/2}}]$	β [1]	b (ph. s^{-1})
cell-bckg.	0.46	1.9×10^4	2.73	4.0×10^{-2}

$$F_2(q_r) = \int_{q_{min}}^{q_{max}} q_r^2 \cdot I_{auto}(q_r)\, dq = \int_{q_{min}}^{q_{max}} \sum_{p=-8}^{0} c_p \cdot q_r^{p+2}\, dq$$
$$= \left(c_{-3} \cdot \ln(q_r) + \sum_{i=-8}^{-4} \frac{1}{i+3} \cdot \frac{c_i}{q_r^{i+3}} + \sum_{i=-2}^{0} \frac{1}{i+3} \cdot \frac{c_i}{q_r^{i+3}} \right) \Bigg|_{q_r=q_{min}}^{q_{max}}, \quad (12)$$

as well as the quadratic displacement $\langle q_r^2 \rangle = F_2(q_r)/F_0(q_r)$ and the experimental limits $I_{auto}(q_{min})$ and $I_{auto}(q_{max})$ of structures that can be resolved. Figure 5(a) shows three freeze-dried cells (cell1–cell3) in dark field contrast mode. The cells exhibit different overall scattering intensities, comprising a relatively strong (cell1, $I_{max}(a, b) \approx 1.5 \times 10^7$ ph. s^{-1}), a moderately (cell2, $I_{max}(a, b) \approx 7.5 \times 10^6$ ph. s^{-1}) and a rather weakly scattering cell (cell3, $I_{max}(a, b) \approx 3.7 \times 10^6$ ph. s^{-1}). *b* a closer look reveals pronounced kinks in the intensity profiles of cell1 and cell2 (see ①and ②), requiring a description based on equation (10) while broad regions of the profile of cell3 (see ③) allow a fitting of the signal to a simple power-law function as defined in equation (7) down to the afore mentioned 0.03 nm^{-1}. For further analysis, we have then applied the automated fitting algorithm to each of the three scan areas: figure 5(c) shows the normalized values of the first four coefficients $c_0^*(a, b)$–$c_{-3}^*(a, b)$ with

$$c_p^*(a, b) = \frac{c_p(a, b)}{\left(\sum_p c_p^2(a, b)\right)^{1/2}}, \quad (13)$$

as a measure for the relative contribution of each c_p to the fit. Results indicate structural differences among the selected cells. The corresponding false color limits for figure 5(c) are given in table 3.

While cell1 and cell2 reveal similar c_p^*-values, results differ for cell3. Figure 5(d) shows the values of c_{-1}^* and c_{-4}^* on a logarithmic scale (with the leading sign coded in color), considering all diffraction patterns within the hatched regions a_1, a_2, a_3 and a_4 as marked in figure 5(a). This shows convincingly, that efficient linear fits to the power-law expansion is capable to treat large datasets in a batch manner, revealing changes which can be confirmed by inspection of the lineshapes 'by eye'.

6. Correlating statistics and structural parameters

Towards a statistically more substantiated interpretation of anisotropic diffraction patterns, we have analyzed a large scan area covering about 1.1 × 1.3 mm of the sample and have computed the respective angular deviation $\Delta\theta(a, b)$ for each pixel (see SI, section 15 for details and section 12 for further examples). Figure 6(a) shows the respective distribution in a histogram. The distribution peaks at $\Delta\theta = 0°$ and decays quickly towards $|\Delta\theta| = 90°$, underlining the pronounced correlation between fluorescence microscopy of labeled actin filaments and anisotropic x-ray diffraction patterns. A t-test with null hypothesis $H_0 : \overline{\Delta\theta} = 0$ yields a t-statistic value $t = -1.09$ and a *p*-value $p = 0.27 > 0.1$, so the null hypothesis cannot be rejected. This is in agreement with our expectation. The observations made can be interpreted in two alternative ways: firstly, the actin fibers could be identified as the dominating scattering contribution, or secondly, the actin filament direction could be interpreted as a polarizing effector for the entire ensemble of scattering biomolecules, resulting in the observed x-ray structure orientation θ_{pa}. Most likely, both explanations may hold some truth. Notwithstanding, the large agreement between such entirely different probes as fluorescence microscopy with labeled f-actin, and scanning SAXS, it is also of interest to have closer look at pixels where the discrepancy is significant.

Interestingly, pixels where the discrepancy is high, are more likely to show moderate or small anisotropy. This finding is substantiated by coding the averaged ω_{pa}-value for each bin in gray value. Of course, high ω_{pa}-values also enable a more accurate determination of θ_{pa}, while results on diffraction patterns with a weak anisotropic character can be influenced significantly by parasitic scattering effects or minor structural attributes within the probed spot. Nevertheless, the conclusion that the angular differences between visible light fluorescence and x-ray data also reflect contributions of further biomolecular assemblies which may not be with the actin filaments is very reasonable.

As computed from the same large scan as the histogram of $\Delta\theta$ above, figure 6(b) shows the results for further structure parameters derived from the x-ray dark field and PCA results. These are the mean overall scattering

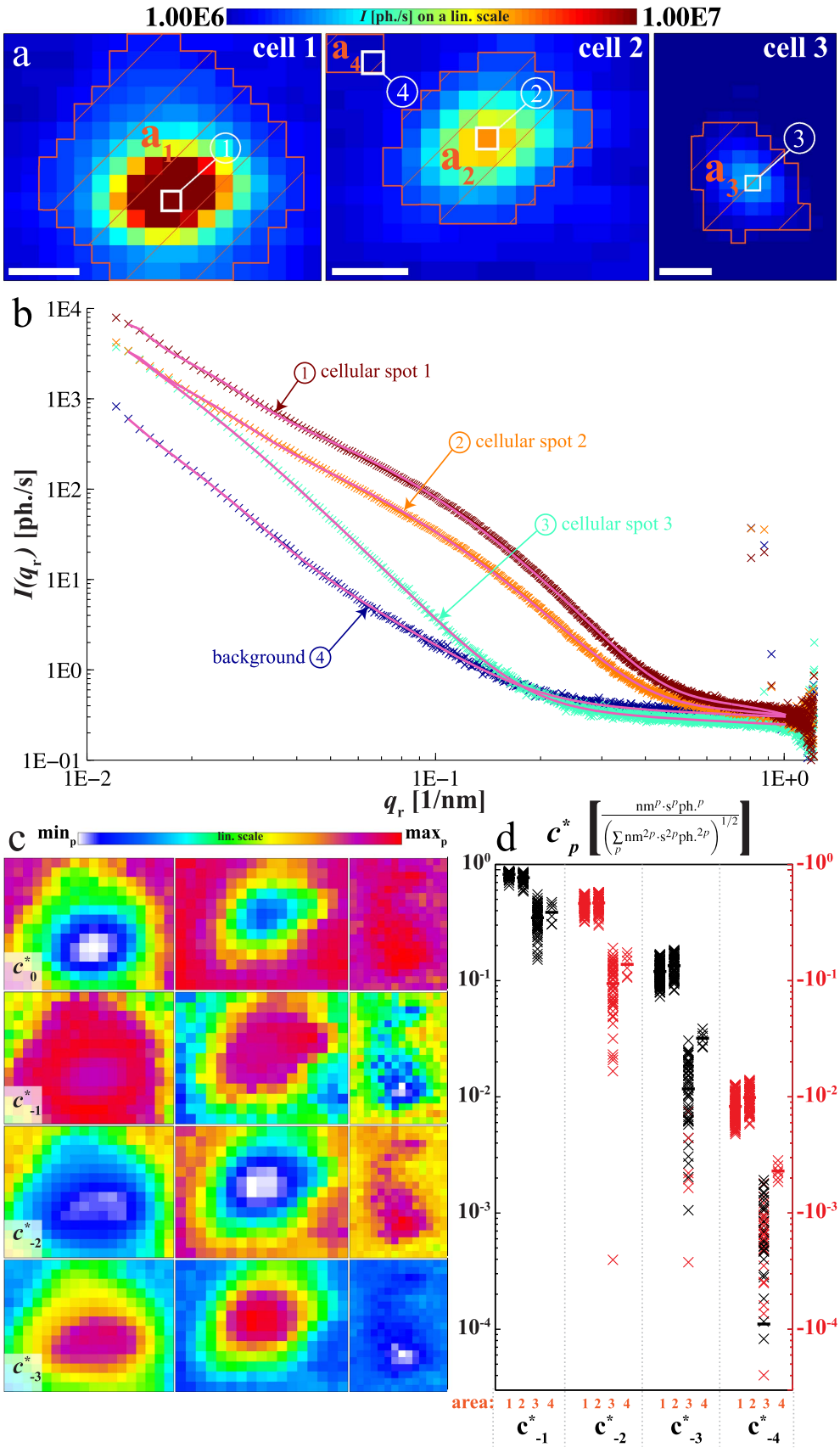

Figure 5. (a) x-ray dark fields of three cells scanned with the micro-SAXS setup. Scalebars: 40 μm. (b) Intensity profiles of selected single spots as marked in *a*. Profiles are fitted to an expansion of power laws $I_{\text{auto}}(q_r)$ as defined in equation (10). (c) Normalized coefficients $c^*_{-3} - c^*_0$ of the three scan regions shown in *a* as defined by equation (13). (d) Statistical analysis of $|c^*_{-4}| - |c^*_{-1}|$ of the hatched areas a_1–a_4 as marked in *a*. Black and red crosses denote positive or negative $c^*_p(a,\ b)$-value, black and red bars mark the respective average values. False color limits for (c) are given in table 3.

Table 3. Limit values for the colorbars used in 5(c) in units of $nm^p\, s^p ph.^p / (\sum_p nm^{2p}\, s^{2p} ph.^{2p})^{1/2}$.

p	Min_p	Max_p
0	-2.6×10^{-1}	9.9×10^{-1}
−1	1.5×10^{-1}	8.8×10^{-1}
−2	-5.8×10^{-1}	-4.0×10^{-4}
−3	-7.4×10^{-3}	1.8×10^{-1}

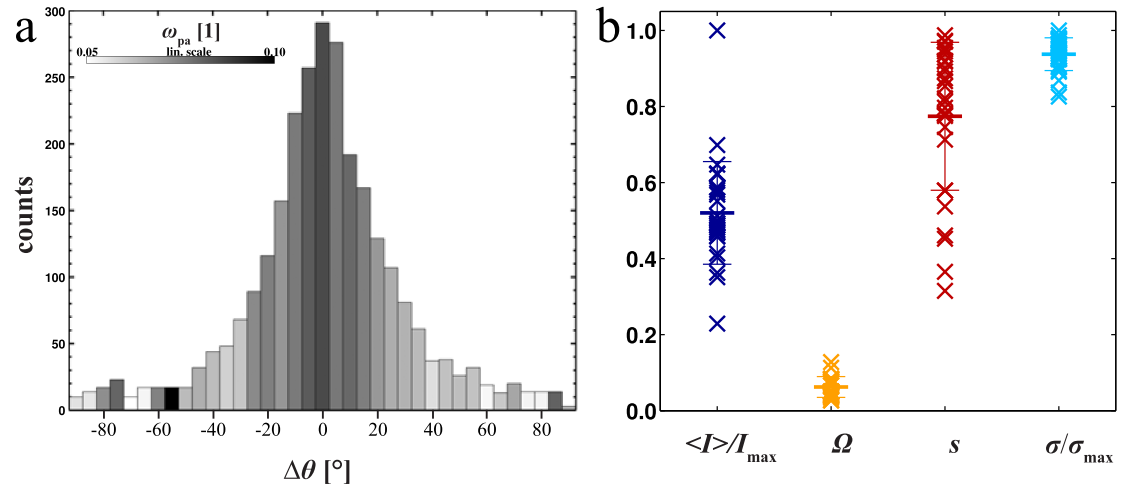

Figure 6. (a) Histogram of the angular deviation $\Delta\theta$ between the orientations computed from fluorescence micrograph and x-ray diffraction patterns, as determined for a large area scan. Results include averaged values for the order parameter ω_{pa} as quantified by PCA (gray scale). (b) Statistical plot of mean scattering intensity $\langle I \rangle$ (each data point represents the mean over one cell), the mean anisotropy $\Omega = \langle \omega_{pa} \rangle$ reflecting the overall degree of the anisotropy (again for each cell), the 2D nematic order parameter s measuring the consistency of orientation directions within a cell, as well as the mean standard deviation of the photon momentum transfer $\langle \bar{\sigma} \rangle$, reflecting the effective sizes of scattering constituents. For definition of these parameters, see [11].

Table 4. Maximum and mean absolut values for $\langle I \rangle$ in (ph. s^{-1}), Ω in [1], s in [1] and $\langle \bar{\sigma} \rangle$ in (1 nm^{-1}).

	Max	Mean
$\langle I \rangle$	9.1×10^6	4.8×10^6
Ω	0.13	0.06
s	0.99	0.77
σ	2.6×10^{-2}	2.4×10^{-2}

intensity $\langle I \rangle$ per cell, the mean order parameter $\Omega = \langle \omega_{pa} \rangle$ of a cell defined as a measure for the overall strength of the anisotropy, the 2D nematic order parameter s as a measure for the consistency of orientation directions within a cell, and the mean standard deviation of the momentum transfer $\langle \bar{\sigma} \rangle$, reflecting the effective sizes of scattering constituents. For details on the definitions of these parameters and their properties, see also [11]. Data points were averaged leading to respective mean values depicted as bars. Comparison to our previous study [11] indicates that the investigated cardiac tissue cells (NRCTCs) have a moderate overall scattering signal $\langle I \rangle$ on the same level as hMSCs or murine myoblasts, a moderate mean order parameter Ω as well as a moderate 2D nematic order parameter s on the same level as naive and muscle-induced hMSCs, but a high mean standard deviation of the momentum transfer $\langle \bar{\sigma} \rangle$, which can be traced back to the line shapes of the radial intensity profiles discussed in section 5 further indicating contributions also from smaller biomolecules or molecular constituents. The average and maximum values of all parameters are listed in table 4. Note, that NRCTCs may be composed of not only CMs but also other celllines as for instance fibroblasts or endothelial cells.

Finally, we have run all procedures described here on the scan shown in figure 2, since this is one well-defined single-cell example with a shape which can be easily inferred from. For the given mask shown in figure 2(i) (white color), a rather weak scattering intensity $\langle I \rangle = 1.84 \times 10^6$ ph. s^{-1} is found, while PCA results lead to a moderate mean orientation $\Omega = 0.09$ for this cell, as well as to a nematic order parameter of $s = 0.86$.

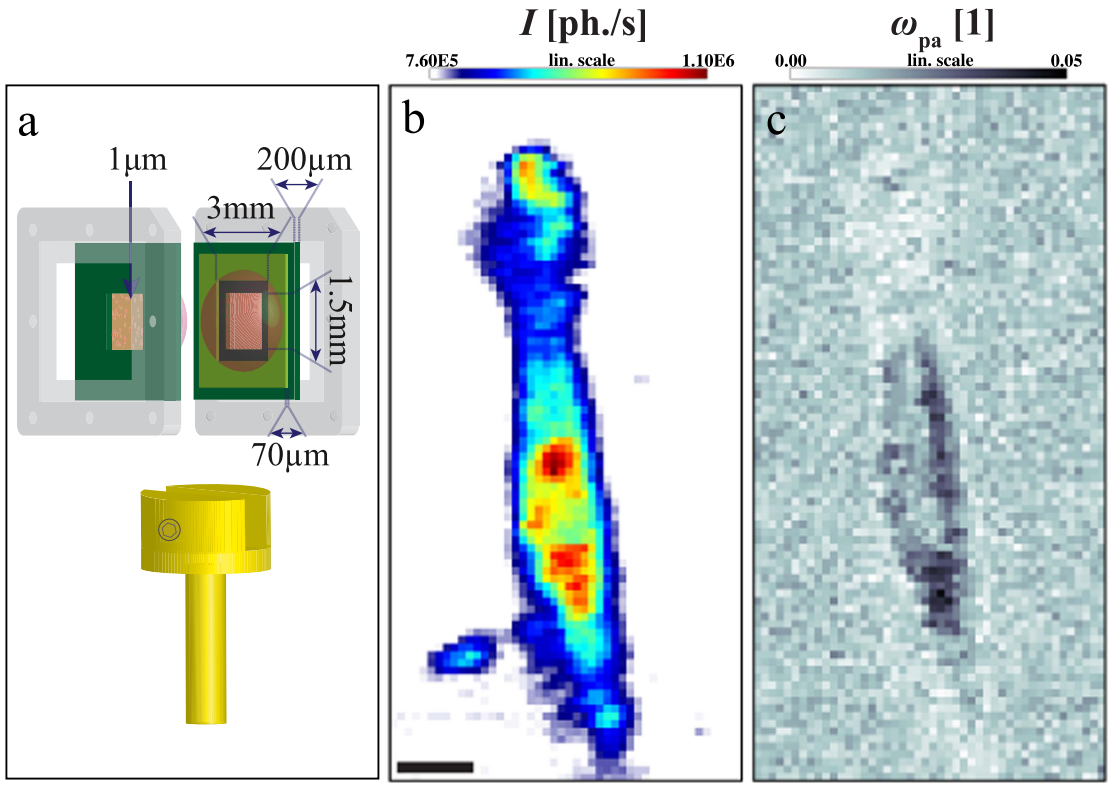

Figure 7. (a) Sketch of a novel wet chamber design (Silson, UK). (b) X-ray dark field obtained for a living cell. Scalebar: 5 μm. (c) PCA-results showing the anisotropy parameter ω_{pa} in gray scale.

Moreover, a comparatively low value for $\langle\bar{\sigma}\rangle = 0.019\ \mathrm{nm}^{-1}$ is found, indicating the predominance of larger structures. Finally, a histogram of the angular deviation is very well in line with the observations stated above (see SI, figure 3).

7. Sample environment and chambers

All of the above results have been obtained on chemically fixed, freeze-dried cells, which can be regarded as a very invasive preparation method, yielding results which may very well be flawed by preparation artifacts. Of course, it is desirable to extend the scanning SAXS methodology to more physiological states and in particular to living cells. To this end, we present a small section to investigate the decrease in signal levels and proof whether the PCA can in principle be extended to data recorded under these conditions.

The first experimental challenge is the design and use of suitable x-ray compatible sample chambers for cells, see also the discussion in [8]. Here we use a simple chamber design based on thin foil window materials with high x-ray transmission and low background. In between foils, on which the cells adhere, the buffer solution assures hydrated conditions for the cell, which is then scanned in either a chemically fixed or the alive state. Especially alive cell recordings are of great interest, since they allow x-ray diffraction experiments under physiological conditions and in future possibly the investigation of dynamic processes, such as contraction of CMs. However, low density contrast between cellular constituents and solution as well as residual scattering caused by the nutrition medium and the chamber windows results in an elevated background signal, so that cellular structural details often remain elusive. Hence, optimized design of chambers is an important issue, see the approaches proposed in [8–10]. Addressing these issues, we have performed first scans on alive cardiac tissue cells kept in a novel wet chamber design (Silson, UK) as sketched in figure 7(a): the chamber comprises two silicon nitride windows with a thickness of 1 μm and a 70 μm spacer with an inner edge length of 3 mm forming a total volume of 0.63 μl. For the photon energy used ($E_{\mathrm{ph.}} = 8.0$ keV), this results in a theoretical transmission of $T = 91\%$ [63].

First scanning SAXS results are presented in figures 7(b)–(c), showing the x-ray dark field map of a cardiac cell in *b*, and the corresponding ω_{pa}-values as obtained by PCA in *c*. Despite the significantly reduced signal level compared to freeze-dried cells, some structural details are revealed. This suggests, that upon further optimization of beam conditions and measurement protocols (scan parameters), the method can be extended to hydrated and alive states of cells.

8. Discussion and outlook

In this work, we have presented scanning mirco- and nano-SAXS diffraction data on disassembled cells isolated from cardiac neonatal rat tissue and prepared in a chemically fixed and freeze-dried, or alive state. The versatility of different synchrotron radiation beamlines and setups [6–10, 50, 56] now enables to study biological cells with selected and variable instrumentation parameters such as photon energy, spot size, scanning step size, q_r-range, x-ray modality (scanning SAXS, x-ray fluorescence, coherent imaging) of samples in different preparation states, ranging from high contrast but artifact-susceptible freeze-dried over vitrified and chemically fixed wet samples to recordings of alive cells.

We have made use of this progress here to perform a correlative study between scanning SAXS in different settings of resolution and q-range and optical fluorescence microscopy. To this end, visible light micrographs recorded at the scan positions during different stages of the preparation process allowed to perform comparative studies considering the structure orientation of filamentous actin θ_{fs} and x-ray structure orientation angles θ_{pa} as determined by automated PCA of cellular diffraction patterns. Thus, we have implemented a modified version of the Filament Sensor [57], which has been adapted in this work to match the pixel size of the fluorescence image to the step size chosen for the x-ray scan. After determining the lateral shifts between the fluorescence image and x-ray dark field, observables θ_{fs} and θ_{pa} could be correlated pixel-by-pixel, enabling the calculation of the local angular deviation $\Delta\theta(a, b) = \theta_{fs}(a, b) - \theta_{pa}(a, b)$. Results indicate a strong correlation of filamentous actin, which is the predominant filamentous structure in eucaryotic cells [64, 65], and anisotropic diffraction patterns of the micro-SAXS scans. This observation first made for a single cell was confirmed by the statistical analysis of a large area micro-SAXS scan. The results also show that cellular areas with a relatively large order parameter ω_{pa} are likely to have a smaller angular deviation $\Delta\theta$.

Furthermore, the degree of anisotropic scattering $\omega_{pa} = |\lambda_1 - \lambda_2|/(\lambda_1 + \lambda_2)$ as first defined in [11] was evaluated as a unitless (order) parameter quantifying the aspect ratio between the variances along both principal axes of the diffraction pattern. This parameter complements the orientation direction θ_{pa} with a measure of how large the scattering is enhanced in this direction. It has also become clear that the anisotropic portion of the diffraction signal cannot be exclusively reduced to the contributions of actin fibers. Instead, the diffraction pattern contain contributions of multiple biomolecular structures. These results were complemented and further refined by nano-SAXS experiments providing a high real space resolution which allowed to assign diffraction patterns to different cellular compartments or areas. Data reveal a rather isotropic character for nucleic diffraction patterns, while diffraction originating from the cytoplasm were found to be more anisotropic including pronounced anisotropy at the cell's perimeter and within long protrusions. Quantifying x-ray diffraction patterns to their anisotropic properties is an essential first step, given the fact that the scattering in particular of polarized cells is highly oriented.

However, this is by far not sufficient to unravel all structural assets, such as local form- and structure factors of a SAXS-scan. As a first step in order to accurately describe local radial intensity profiles $I(q_r)$, we have implemented a general fitting ansatz considering a linear combination of q_r^p with fixed integer exponents, which was found to reliably describe cellular SAXS signals even over a broad q_r-range, covering about two orders in reciprocal space. When implemented in an automated scheme, this approach reduces the description of all intensity profiles of a SAXS scan to nine observables, namely the nine coefficients c_p of equation (10) with $p \in [-8, 0]$, $p \in \mathbb{Z}$. This reduction is at this point purely empirical, but observables of the structure factor could easily be computed from the fitted coefficients, either analytically or numerically. The description thus seems quite complete as far as the data is concerned. In future, the space of structure factor coefficients and the two-dimensional space of the scanned area could also be analyzed in view of advanced linear algebra tools, eigen structure-factors and eigen-images, similar to what has become state of the art in spectromicroscopy [66, 67]. In this way, the number and spatial distribution of structural constituents could be identified in an automated manner.

While this goal is beyond the scope of the present work, we have already started to extend the statistical analysis, and computed maps of the observables scattering intensity $\langle I \rangle$, mean orientation Ω, nematic order parameter s, and second moment of the scattering distribution $\langle \bar{\sigma} \rangle$. Compared to previous cells [11], cardiac cells studied here were not at all exceptional. They were found to exhibit a moderate average scattering intensity $\langle I \rangle$, a rather weak average anisotropy Ω, a moderate order parameter s, but a comparatively large standard deviation of the momentum transfer $\langle \bar{\sigma} \rangle$. Concerning $\langle I \rangle$ and Ω, observations can be recognized already by direct comparison of diffraction patterns, see e. g. SI figure 5). Moreover, data shown in section 6 and SI section 15 reveal a strong visible light fluorescence signal outlining the cortex but also varying fiber directions within cellular regions. Since θ_{fs} and θ_{pa} were found to be highly correlated, this entails that orientational fluctuations within single cells cause the comparatively low values for s.

Next, let us comment on the possibility of distinguishing different cell types by scanning SAXS. It is commonly accepted that different cell lines exhibit different characteristic structural attributes. It can therefore

be expected, that when choosing an appropriate q-range, such structural differences could manifest themselves in form of different cellular x-ray diffraction signals. In case of the cardiac tissue cells presented in this work, not only CMs but also other cell types such as fibroblasts and endothelial cells are present [51, 68–70]. The distribution of the order parameter s in figure 6 could be indicative for a bi-modal distribution resulting from different cell types of a mixed culture. In this case, s would be a candidate for suitable cell type markers. Furthermore, we attribute the relatively high values for $\langle\bar{\sigma}\rangle$ to a kink-region, as further described in section 5. Important for such an identification by robust and automated analysis, is an algorithm which can reduced the data to a set of essential structural coefficients amenable to further treatment by linear algebra methods (such as diagonalization, identification of basis systems, cluster analysis, principle components, and various other transformations). Finally, we have addressed the issue of hydrated and alive cell recordings, which pose a much higher challenge. This included technical issues such as the design of a wet chamber that is applicable to cell cultivation but at the same time has low background. Here, we have introduced chambers based on two ultrathin silicon nitride windows with 70 μm spacing appropriate for (initially) alive cells. The scanned cells revealed a clear signal in the x-ray dark field enabling the identification of nucleic and cytoplasmic areas as well as substructures within cellular diffraction patterns which could be tracked by PCA. However, radiation induced damage by the x-ray beam is a major concern. While it is clear that the cell cannot survive, the central question is whether structural integrity in a given scan point can be warranted at least for the time scale of the dwell time, and whether spread of damage can be controlled. For example, the dose in some of the nanofocus experiments, for example scan of figure 7 was as high as $D \approx 2.1 \times 10^8$ Gy. Overlap between neigboring pixels must clearly be avoided. In future, the dose can be further reduced by simple experimental measures: increasing the transmission of photon transport from the cell to the detector, i.e. higher window transmission, eventually reducing channel dimensions, and evacuating a flight path. Detector efficiency is a further important parameter. However, in sum we estimate that these parameters can only amount to a dose reduction by possibly a factor of 5. More improvement can be provided by cleaning the beam profile and reducing the background, since higher signal-to-noise would allow us to reduce the intensity significantly. Further, it can be very beneficial to flush the chamber in order to keep the concentration of free radials low. In summary, we have studied the local structures of cardiac myofibrils in single cells using state of the art x-ray focussing of synchrotron radiation. In particular, the automated data analysis as performed here is an important step towards the quantification of cellular SAXS diffraction signals. Further investigation will embed this work in a larger context complementing data by simulations and broad q_r-range nano-SAXS recordings. The approach presented here should thus contribute to the long term goal of extending macroscopic muscle diffraction studies to the level of single muscle cells. Beyond muscle cells, we should also point out the general opportunities of measuring structural anisotropies at the nanoscale in biological cells over large areas.

Acknowledgments

We thank Susanne Hengst, Kristin Müller and Julia Scherber for additional sample preparation and technical support in cell culture, Ana Diaz providing expertise and local contact at the cSAXS beamline, Michael Sprung for expertise and support at the P10 beamline, Markus Osterhoff and Marius Priebe for help during beamtime and for related collaborations, and Sarah Köster for advice in particular on the issue of sample chambers and preparation of cells. Markus Osterhoff is also acknowledged for helpful discussions on data analysis and numerical work. Moreover, we thank the group of Stefan Luther (MPI for dynamics and self-organisation), in particular Tina Althaus, Marion Kunze, Claudia Richter and Stefan Luther as well as Marco Tarantola for providing and preparing the NRCTCs for the work presented here as well as a scientific feedback whenever we had issues to discuss. Financial support was primarily provided by Deutsche Forschungsgemeinschaft through grant DFG/SFB 937, project A11, but also took advantage of method development funded by DFG/SFB755, project B08.

Author contribution

TS and FR designed research.MEprepared micro-SAXS samples. MB and JDN prepared nano-SAXS samples. MB established sample preparation workflow. TS, MB, JDN concepted and implemented the beamline setup. MB, JDN, ME, TS, FR prepared the beamtime and recorded data. MB analyzed data. BE developed and adaptedthe filament sensor for fluroescence images. TS and FR provided continuous scientific supervision and advice. MB and TS wrote the manuscript, with contributions from BE, and corrections from all authors.

References

[1] Bras W, Koizumi S and Terrill N J 2014 Beyond simple small-angle x-ray scattering: developments in online complementary techniques and sample environments *Int. Union Crystallogr. J.* **1** 478–91
[2] Irving T C and Maughan D W 2000 In vivo x-ray diffraction of indirect flight muscle from drosophila melanogaster *Biophys. J.* **78** 2511–5
[3] Huxley A 1988 Prefatory chapter: muscular contraction *Alln. Rev. Physiol.* **50** 1–16
[4] Huxley H E, Simmons R M, Faruqi A R, Kress M, Bordas J and Koch M H J 1983 Changes in the x-ray reflections from contracting muscle during rapid mechanical transients and their structural implications *J. Mol. Biol.* **169** 469–506
[5] Kress M, Huxley H E, Faruqi A R and Hendrix J 1986 Structural changes during activation of frog muscle studied by time-resolved x-ray diffraction *J. Mol. Biol.* **188** 325–42
[6] Wilke R N, Priebe M, Bartels M, Giewekemeyer K, Diaz A, Karvinen P and Salditt T 2012 Hard x-ray imaging of bacterial cells: nano-diffraction and ptychographic reconstruction *Opt. Express* **20** 19232–54
[7] Weinhausen B, Nolting J- F, Olendrowitz C, Langfahl-Klabes J, Reynolds M, Salditt T and Köster S 2012 x-ray nano-diffraction on cytoskeletal networks *New J. Phys.* **14** 085013
[8] Weinhausen B and Köster S 2013 Microfluidic devices for x-ray studies on hydrated cells *Lab Chip* **13** 212–5
[9] Weinhausen B, Saldanha O, Wilke R N, Dammann C, Priebe M, Burghammer M, Sprung M and Köster S 2014 Scanning x-ray nanodiffraction on living eukaryotic cells in microfluidic environments *Phys. Rev. Lett.* **112** 088102
[10] Priebe M, Bernhardt M, Blum C, Tarantola M, Bodenschatz E and Salditt T 2014 Scanning x-ray nanodiffraction on dictyostelium discoideum *Biophys. J.* **107** 2662–73
[11] Bernhardt M, Priebe M, Osterhoff M, Wollnik C, Diaz A, Salditt T and Rehfeldt F 2016 X-ray micro- and nanodiffraction imaging on human mesenchymal stem cells and differentiated cells *Biophys. J.* **110** 680–90
[12] Bausch A R and Schwarz U S 2013 Cellular mechanosensing: sharing the force *Nat. Mater.* **12** 948–9
[13] Engler A J, Sen S, Sweeney H L and Discher D E 2006 Matrix elasticity directs stem cell lineage specification *Cell* **126** 677–89
[14] Zemel A, Rehfeldt F, Brown A E X, Discher D E and Safran S A 2010 Optimal matrix rigidity for stress-fibre polarization in stem cells *Nat. Phys.* **6** 468–73
[15] Kohler S, Schaller V and Bausch A R 2011 Structure formation in active networks *Nat. Mater.* **10** 462–8
[16] Huxley H E 1996 A personal view of muscle and motility mechanisms *Annu. Rev. Physiol.* **58** 1–9
[17] Huxley H E 2004 Fifty years of muscle and the sliding filament hypothesis *Eur. J. Biochem.* **271** 1403–15
[18] Huxley H and Hanson J 1954 Changes in the cross-striations of muscle during contraction and stretch and their structural interpretation *Nature* **173** 973–6
[19] Huxley A F and Niedergerke R 1954 Structural changes in muscle during contraction *Nature* **173** 971–3
[20] Huxley H E 1969 The mechanism of muscular contraction *Science* **164** 1356–66
[21] Hynes T R, Block S M, White B T and Spudich J A 1987 Movement of myosin fragments in vitro: domains involved in force production *Cell* **48** 953–63
[22] Lorand L 1953 Adenosine triphosphate-creatine transphosphorylase as relaxing factor of muscle *Nature* **172** 1181–3
[23] Spudich J A 2001 The myosin swinging cross-bridge model *Nat. Rev. Mol. Cell Biol.* **2** 387–92
[24] Stangl J, Mocuta C, Chamard V and Carbone D 2013 *Nanobeam X-Ray Scattering: Probing Matter at the Nanoscale* (Weinheim: Wiley)
[25] Jefimovs K, Bunk O, Pfeiffer F, Grolimund D, van der Veen J F and David C 2007 Fabrication of fresnel zone plates for hard x-rays *Microelectron. Eng.* **84** 1467–70
[26] Snigirev A, Kohn V, Snigireva I and Lengeler B 1996 A compound refractive lens for focusing high-energy x-rays *Nature* **384** 49–51
[27] Schroer C G, Kurapova O, Patommel J, Boye P, Feldkamp J, Lengeler B, Burghammer M, Riekel C, Vincze L, van der Hart A and Kuchler M 2005 Hard x-ray nanoprobe based on refractive x-ray lenses *Appl. Phys. Lett.* **87** 124103
[28] Schroer C G and Lengeler B 2005 Focusing hard x rays to nanometer dimensions by adiabatically focusing lenses *Phys. Rev. Lett.* **94** 054802
[29] Hignette O, Cloetens P, Rostaing G, Bernard P and Morawe C 2005 Efficient sub 100 nm focusing of hard x rays *Rev. Sci. Instrum.* **76** 063709
[30] Mimura H *et al* 2007 Efficient focusing of hard x rays to 25 nm by a total reflection mirror *Appl. Phys. Lett.* **90** 051903
[31] Mimura H *et al* 2010 Breaking the 10 nm barrier in hard-x-ray focusing *Nat. Phys.* **6** 122–5
[32] Salditt T, Kalbfleisch S, Osterhoff M, Krüger S P, Bartels M, Giewekemeyer K, Neubauer H and Sprung M 2011 Partially coherent nano-focused x-ray radiation characterized by Talbot interferometry *Opt. Express* **19** 9656–75
[33] Fratzl P, Fratzl-Zelman N, Klaushofer K, Vogl G and Koller K 1991 Nucleation and growth of mineral crystals in bone studied by small-angle x-ray scattering *Calcif. Tissue Int.* **48** 407–13
[34] Fratzl P, Gupta H S, Paschalis E P and Roschger P 2004 Structure and mechanical quality of the collagen-mineral nano-composite in bone *J. Mater. Chem.* **14** 2115–23
[35] Lichtenegger H, Reiterer A, Stanzl-Tschegg S E and Fratzl P 1999 Variation of cellulose microfibril angles in softwoods and hardwoods-a possible strategy of mechanical optimization *J. Struct. Biol.* **128** 257–69
[36] Pabisch S, Wagermaier W, Zander T, Li C and Fratzl P 2013 Imaging the nanostructure of bone and dentin through small- and wide-angle x-ray scattering *Meth. Enzymol.* **532** 391–413
[37] Kerschnitzki M, Kollmannsberger P, Burghammer M, Duda G N, Weinkamer R, Wagermaier W and Fratzl P 2013 Architecture of the osteocyte network correlates with bone material quality *J. Bone Miner. Res.* **28** 1837–45
[38] Fratzl P 2015 Imaging techniques: extra dimension for bone analysis *Nature* **527** 308–9
[39] Morgan A J *et al* 2015 High numerical aperture multilayer laue lenses *Sci. Rep.* **5** 9892
[40] Döring F *et al* 2013 Sub-5 nm hard x-ray point focusing by a combined Birkpatrick–Baez mirror and multilayer zone plate *Opt. Express* **21** 19311–23
[41] Hemonnot C Y, Mauermann M, Herrmann H and Köster S 2015 Assembly of simple epithelial keratin filaments: deciphering the ion dependence in filament organization *Biomacromolecules* **16** 3313–21
[42] Strzalka J 2014 Cellular diffraction: scanning x-ray nanodiffraction from living cells *Biophys. J.* **107** 2489
[43] Kornreich M, Avinery R and Beck R 2013 Modern x-ray scattering studies of complex biological systems *Curr. Opin. Biotechnol.* **24** 716–23
[44] Wilke R N, Hoppert M, Krenkel M, Bartels M and Salditt T 2015 Quantitative x-ray phase contrast waveguide imaging of bacterial endospores *J. Appl. Crystallogr* **48** 464–76

[45] Klar T A, Jakobs S, Dyba M, Egner A and Hell S W 2000 Fluorescence microscopy with diffraction resolution barrier broken by stimulated emission *Proc. Natl Acad. Sci. USA* **97** 8206–10
[46] Westphal V and Hell S W 2005 Nanoscale resolution in the focal plane of an optical microscope *Phys. Rev. Lett.* **94** 143903
[47] Hess S T, Girirajan T P and Mason M D 2006 Ultra-high resolution imaging by fluorescence photoactivation localization microscopy *Biophys. J.* **91** 4258–72
[48] Betzig E, Patterson G H, Sougrat R, Lindwasser O W, Olenych S, Bonifacino J S, Davidson M W, Lippincott-Schwartz J and Hess H F 2006 Imaging intracellular fluorescent proteins at nanometer resolution *Science* **313** 1642–5
[49] Rust M J, Bates M and Zhuang X 2006 Sub-diffraction-limit imaging by stochastic optical reconstruction microscopy (STORM) *Nat. Methods* **3** 793–5
[50] Salditt T, Osterhoff M, Krenkel M, Wilke R N, Priebe M, Bartels M, Kalbfleisch S and Sprung M 2015 Compound focusing mirror and x-ray waveguide optics for coherent imaging and nano-diffraction *J. Synchrotron Radiat.* **22** 867–78
[51] Rother J, Richter C, Turco L, Knoch F, Mey I, Luther S, Janshoff A, Bodenschatz E and Tarantola M 2015 Crosstalk of cardiomyocytes and fibroblasts in co-cultures *R. Soc.* **5** 1–0
[52] Richter C, Christoph J, Lehnart S E and Luther S 2016 Optogenetic light crafting tools for the control of cardiac arrhythmias *Methods Mol. Biol.* **1408** 293–302
[53] Takahashi Y, Suzuki A, Zettsu N, Oroguchi T, Takayama Y, Sekiguchi Y, Kobayashi A, Yamamoto M and Nakasako M 2013 Coherent diffraction imaging analysis of shape-controlled nanoparticles with focused hard x-ray free-electron laser pulses *Nano Lett.* **13** 6028–32
[54] http://silson.com
[55] Henrich B, Bergamaschi A, Broennimann C, Dinapoli R, Eikenberry E F, Johnson I, Kobas M, Kraft P, Mozzanica A and Schmitt B 2009 Pilatus: a single photon counting pixel detector for x-ray applications *Radiation Imaging Detectors 2008 Proc. 10th Int. Workshop on Radiation Imaging Detectors; Nucl. Instrum. Methods Phys. Res.* A **607** 247– 249
[56] Töpperwien M, Priebe M and Salditt T 2016 Actin bundles cross-linked with alpha-actinin studied by nanobeam x-ray diffraction *Eur. Biophys. J.* **45** 383–92
[57] Eltzner B, Wollnik C, Gottschlich C, Huckemann S and Rehfeldt F 2015 The filament sensor for near real-time detection of cytoskeletal fiber structures *PLoS One* **10** e0126346 05
[58] Hotz T and Huckemann S 2015 Intrinsic means on the circle: uniqueness, locus and asymptotics *S. Ann. Inst. Stat. Math.* **67** 177
[59] Szekely P, Ginsburg A, Ben-Nun T and Raviv U 2010 Solution x-ray scattering form factors of supramolecular self-assembled structures *Langmuir* **26** 13110–29
[60] Brennich M E, Bauch S, Vainio U, Wedig T, Herrmann H and Koster S 2014 Impact of ion valency on the assembly of vimentin studied by quantitative small angle x-ray scattering *Soft Matter* **10** 2059–68
[61] Squire J M, Al-Khayat H A and Yagi N 1993 Muscle thin-filament structure and regulation *J. Chem. Soc. Faraday Trans.* **89** 2717–26
[62] Al-Khayat H A, Yagi N and Squire J M 1995 Structural changes in actin-tropomyosin during muscle regulation: computer modelling of low-angle x-ray diffraction data *J. Mol. Biol.* **252** 611–32
[63] Lawrence Berkeley National Laboratory *The center for x-ray optics (cxro)* (www.cxro.lbl.gov) (Accessed: 17 February 2016)
[64] Luby-Phelps K 2000 Cytoarchitecture and physical properties of cytoplasm: vol, viscosity, diffusion, intracellular surface area *Int. Rev. Cytol.* **192** 189–221
[65] Bray D and Thomas C 1975 The actin content of fibroblasts *Biochem. J.* **147** 221–8
[66] Lerotic M, Jacobsen C, Schr T and Vogt S 2004 Cluster analysis of soft x-ray spectromicroscopy data *Ultramicroscopy* **100** 35–57
[67] Lerotic M, Jacobsen C, Gillow J B, Francis A J, Wirick S, Vogt S and Maser J 2005 Cluster analysis in soft x-ray spectromicroscopy: finding the patterns in complex specimens *Proc. 14th Int. Conf. on Vacuum Ultraviolet Radiation Physics; J. Electron Spectrosc. Relat. Phenom.* **144-147** 1137–43
[68] Murry C E, Field L J and Menasché P 2005 Cell-based cardiac repair reflections at the 10 year point *Circulation* **112** 3174–83
[69] Banerjee I, Fuseler J W, Price R L, Borg T K and Baudino T A 2007 Determination of cell types and numbers during cardiac development in the neonatal and adult rat and mouse *Am. J. Physiol. Heart Circ. Physiol.* **293** H1883–91
[70] Bianconi E *et al* 2013 An estimation of the number of cells in the human body *Ann. Hum. Biol.* **40** 463–71